

Host-dependent Eu^{2+}/Eu^{3+} co-luminescence and excitation-tunable multicolor emission of Eu-doped AeF_2 (Ae = Ca, Sr, Ba, $Ca_{0.5}Sr_{0.5}$, $Ca_{0.33}Sr_{0.33}Ba_{0.33}$) single crystals

Xiaobo Huang(黄孝波), Ying Quan(全颖), Wudi Wang(王无敌), Qingguo Wang(王庆国), Xiaodong Xu(徐晓东), Huili Tang(唐慧丽), and Jun Xu(徐军)

Citation: Chin. Phys. B, 2026, 35 (**4**): 048102. DOI: 10.1088/1674-1056/ae0562
http://cpb.iphy.ac.cn; http://iopscience.iop.org/cpb

What follows is a list of articles you may be interested in

High pressure growth of transition-metal monosilicide RhGe single crystals

Xiangjiang Dong(董祥江), Bowen Zhang(张博文), Xubin Ye(叶旭斌), Peng Wei(魏鹏), Lei Lian(廉磊), Ning Sun(孙宁), Youwen Long(龙有文), Shangjie Tian(田尚杰), Shouguo Wang(王守国), Hechang Lei(雷和畅), and Runze Yu(于润泽)

Chin. Phys. B, 2025, 34 (**8**): 088101. DOI: 10.1088/1674-1056/add7ab

Single crystal growth and characterization of 166-type magnetic kagome metals

Huangyu Wu(吴黄宇), Jinjin Liu(刘锦锦), Yongkai Li(李永恺), Peng Zhu(朱鹏), Liu Yang(杨柳), Fuhong Chen(陈富红), Deng Hu(胡灯), and Zhiwei Wang(王秩伟)

Chin. Phys. B, 2024, 33 (**9**): 098101. DOI: 10.1088/1674-1056/ad553b

Single crystal growth and transport properties of narrow-bandgap semiconductor RhP_2

De-Sheng Wu(吴德胜), Ping Zheng(郑萍), and Jian-Lin Luo(雒建林)

Chin. Phys. B, 2024, 33 (**8**): 088101. DOI: 10.1088/1674-1056/ad4cd5

Synthesis and nitrogen content regulation of diamond in a high-pressure hydrogen-rich environment

Guofeng Huang(黄国锋), Liangchao Chen(陈良超), and Chao Fang(房超)

Chin. Phys. B, 2024, 33 (**6**): 068102. DOI: 10.1088/1674-1056/ad2a6d

Fluorescence spectra of colloidal self-assembled CdSe nano-wire on substrate of porous Al_2O_3/Au nanoparticles

Xin Zhang(张欣), Li-Ping Shao(邵丽萍), Man Peng(彭嫚), Zhong-Chen Bai(白忠臣), Zheng-Ping Zhang(张正平), Shui-Jie Qin(秦水介)

Chin. Phys. B, 2019, 28 (**6**): 068103. DOI: 10.1088/1674-1056/28/6/068103

Host-dependent Eu^{2+}/Eu^{3+} co-luminescence and excitation-tunable multicolor emission of Eu-doped AeF_2 ($Ae =$ Ca, Sr, Ba, $Ca_{0.5}Sr_{0.5}$, $Ca_{0.33}Sr_{0.33}Ba_{0.33}$) single crystals

Xiaobo Huang(黄孝波)[1], Ying Quan(全颖)[1], Wudi Wang(王无敌)[1,†], Qingguo Wang(王庆国)[1,‡], Xiaodong Xu(徐晓东)[2], Huili Tang(唐慧丽)[1], and Jun Xu(徐军)[1]

[1] *MOE Key Laboratory of Advanced Micro-Structured Materials, School of Physics Science and Engineering, Institute for Advanced Study, Tongji University, Shanghai* 200092, *China*

[2] *Jiangsu Key Laboratory of Advanced Laser Materials and Devices, School of Physics and Electronic Engineering, Jiangsu Normal University, Xuzhou* 221116, *China*

(Received 12 May 2025; revised manuscript received 27 August 2025; accepted manuscript online 10 September 2025)

This study successfully grew a series of mixed-valence Eu^{2+}/Eu^{3+} co-activated alkaline-earth fluoride single crystals (CaF_2, SrF_2, BaF_2, $Ca_{0.5}Sr_{0.5}F_2$, and the medium-entropy $Ca_{0.33}Sr_{0.33}Ba_{0.33}F_2$) using the vertical Bridgman method. During the high-temperature growth process, Eu^{3+} undergoes spontaneous reduction to form Eu^{2+}. X-ray photoelectron spectroscopy (XPS) confirmed the coexistence of both valence states, and their relative ratio exhibits a strong host-dependence; for instance, Eu^{2+} is predominant in SrF_2, while Eu^{3+} is dominant in BaF_2. Under ultraviolet excitation, all crystals simultaneously exhibit the broadband emission of Eu^{2+} (400–550 nm) and the narrow-line emission of Eu^{3+} (585–710 nm). The Eu^{2+} emission peak systematically red-shifts from 440 nm in CaF_2 to 485 nm in BaF_2 as the host cation radius increases. Efficient resonant energy transfer from Eu^{2+} to Eu^{3+} is evidenced by spectral overlap and opposing fluorescence lifetime trends. By controlling the host's composition, the emission chromaticity of the crystals can be continuously tuned from the deep-blue of CaF_2 (0.1720, 0.0382) to the warm-white of BaF_2 (0.4135, 0.3516) under 299 nm excitation. Notably, the medium-entropy Eu: $Ca_{0.33}Sr_{0.33}Ba_{0.33}F_2$ crystal can achieve a shift in emission tone from neutral white to warm white simply by changing the excitation wavelength. These findings provide a new design strategy for developing single-activator, wide-gamut, tunable luminescent materials for next-generation solid-state lighting and display technologies.

Keywords: matrix effect, Eu^{2+}/Eu^{3+}, energy transfer, multicolor emission, Eu:AeF_2 crystals

PACS: 81.10.–h, 87.15.mq, 87.16.dt

DOI: 10.1088/1674-1056/ae0562 **CSTR:** 32038.14.CPB.ae0562

1. Introduction

Eu-doped luminescent materials have attracted considerable attention owing to their distinctive optical properties, and have therefore been extensively investigated in host matrices such as alkaline-earth metal fluorides, silicates, and aluminates. These phosphors have been widely explored for applications in LED displays, temperature sensing, and optical communication.[1–8] In most compounds, europium occurs as Eu^{3+} and Eu^{2+}. Eu^{2+} exhibits a broad $4f^65d^1 \rightarrow 4f^7$emission band extending from ultraviolet to near-infrared.[9–12] The position of this band is strongly governed by the crystal-field strength generated by the ligands, which in turn depends on factors such as the charge, ionic radius, and bonding character of the host matrix and of any co-dopants. Consequently, appropriate choice of the host enables precise tuning of Eu^{2+} luminescence.[13–15]

For Eu^{3+} ions, electric dipole transitions primarily occur at wavelengths between 610–620 nm, while magnetic dipole transitions are centered near 590 nm.[16–18] Compared with Eu^{2+}, Eu^{3+} luminescence is less sensitive to the host matrix. Europium ions are typically introduced via compounds such as EuF_3 or Eu_2O_3, with Eu^{3+} being the dominant form. The reduction of Eu^{3+} to Eu^{2+} often requires high-temperature reducing atmospheres (e.g., N_2, H_2 or CO),[19–31] making it challenging to obtain Eu^{2+}. In Eu:AeF_2 ($Ae =$ Ca, Sr, Ba, $Ca_{0.5}Sr_{0.5}$, $Ca_{0.33}Sr_{0.33}Ba_{0.33}$), Eu^{3+} ions achieve charge compensation through interstitial fluoride ions.[32–35] These interstitial ions can either maintain cubic symmetry when distant or alter the local symmetry when in proximity. Consequently, the luminescent spectra can be tuned by varying the Eu^{3+} concentration and selecting different matrices.[36–40] Furthermore, there is spectral overlap between the excitation spectra of Eu^{3+} and the emission spectra of Eu^{2+}, enabling efficient $Eu^{2+} \rightarrow Eu^{3+}$ energy transfer,[41–49] which can significantly influence the emission spectra of Eu:AeF_2.

Systematic investigations of high-quality Eu^{2+}/Eu^{3+} co-doped single crystals are still lacking, and single-crystal systems can eliminate interference from extrinsic factors such as grain boundaries and surfaces. In addition, the application of

†Corresponding author. E-mail: 25310031@tongji.edu.cn

‡Corresponding author. E-mail: wqingguo_83@yahoo.com.cn

© 2026 Chinese Physical Society and IOP Publishing Ltd. All rights, including for text and data mining, AI training, and similar technologies, are reserved.

medium-entropy design principles to tune the redox equilibrium and energy transfer in fluoride single crystals has not yet been reported.

Eu:AeF$_2$ (Ae = Ca, Sr, Ba, Ca$_{0.5}$Sr$_{0.5}$, Ca$_{0.33}$Sr$_{0.33}$Ba$_{0.33}$) single crystals were grown by the vacuum vertical-Bridgman method. Under 299 nm excitation, they display the broad Eu^{2+} 4f^{6}5d^1 $\rightarrow$ 4f^7 band (400–550 nm) together with the sharp Eu^{3+} ^{5}D$_0$ $\rightarrow$ ^{7}F$_J$ lines (585–710 nm). The Eu^{2+} maximum red-shifts from 440 nm in CaF$_2$ to 485 nm in BaF$_2$ as the host polarizability increases, while Eu^{3+} emission concomitantly intensifies, enabling chromaticity tuning from deep-blue ($x = 0.172$, $y = 0.038$) to warm-white ($x = 0.414$, $y = 0.352$). Substantial spectral overlap between the Eu^{2+} emission and Eu^{3+} excitation bands, together with opposite trends in their lifetimes τ Eu^{2+} shortens while τ Eu^{3+} lengthens with increasing Eu content, confirms efficient resonant Eu^{2+} $\rightarrow$ Eu^{3+} energy transfer. These results demonstrate that host-dependent Eu^{2+}/Eu^{3+} co-luminescence affords a single-activator route to excitation-tunable multicolor emission in fluoride single crystals.

2. Experimental methods

AeF$_2$ (Ae = Ca, Sr, Ba, Ca$_{0.5}$Sr$_{0.5}$, Ca$_{0.33}$Sr$_{0.33}$Ba$_{0.33}$) single crystals were grown with different molar Eu fractions ($X = 0.3$ %mol, 0.6 %mol, 1 %mol) by the vertical Bridgman technique. High-purity CaF$_2$, SrF$_2$, BaF$_2$ (99.999 %mol), and EuF$_3$ (99.999 %mol) powders served as starting materials. The powders were thoroughly mixed, loaded into a porous graphite crucible, and grown under near-vacuum conditions ($\sim$ 2 Pa) to suppress oxidation. All crystals were produced in the same growth run to ensure consistency, and were then polished into 1 mm-thick circular slices for measurement.

X-ray diffraction (XRD) patterns were recorded on a Bruker diffractometer (Cu K_{α_1}, $\lambda = 0.154060$ nm). Inductively coupled plasma atomic-emission spectroscopy (ICP-AES) quantified the dopant concentrations. X-ray photoelectron spectroscopy (XPS) was performed on an ESCALAB 250 (energy resolution 0.5 eV) after argon-ion etching (2 kV, 10 s). Fluorescence spectroscopy measured excitation and emission spectra and fluorescence lifetimes on an Edinburgh FLS920, using a xenon-lamp excitation source and a PMT detector. Identical testing conditions were maintained for all samples to ensure comparability.

3. Results and discussion

The grown Eu:AeF$_2$ (Ae = Ca, Sr, Ba, Ca$_{0.5}$Sr$_{0.5}$, Ca$_{0.33}$Sr$_{0.33}$Ba$_{0.33}$) single crystals are shown in Fig. 1(a). Samples for spectroscopic measurements were processed into 1 mm-thick, double-sided polished circular slices. Using SrF$_2$ as an example, the crystal structure of Eu:SrF$_2$ was visualized with VESTA software, as shown in Fig. 1(b). Alkaline-earth fluoride crystals belong to the cubic crystal system, with a face-centered cubic (FCC) configuration and space group of $Fm\bar{3}m$.

Each Ae^{2+} ion is surrounded by eight F$^-$ ions, forming an anion-centered cubic coordination polyhedron. Each F$^-$ ion is surrounded by four Ae^{2+} ions, creating a cation-centered tetrahedral coordination. The Ae^{2+} ions occupy face-centered matrix sites, forming a closely packed structure. Both Eu^{2+} and Eu^{3+} ions substitute at Ae^{2+} matrix positions.

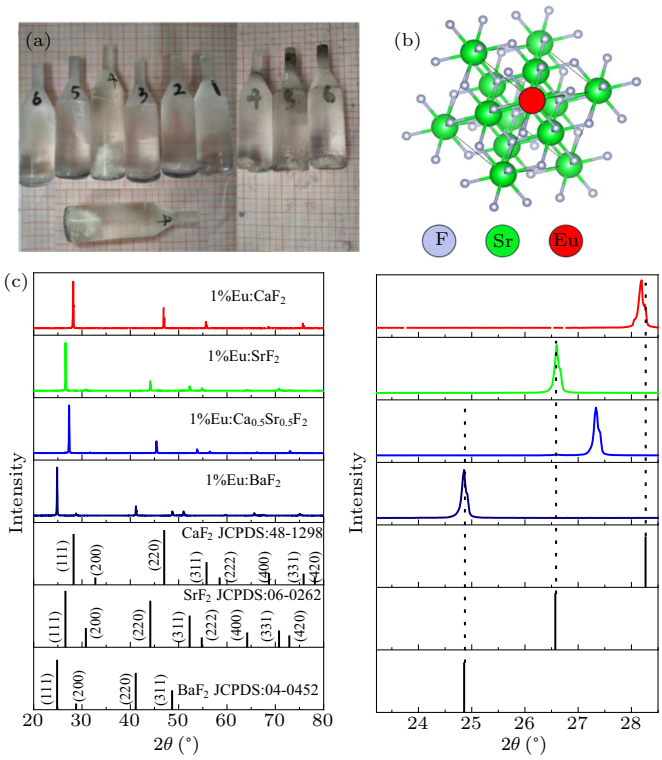


Fig. 1. (a) Photograph of Eu:AeF$_2$ (Ae = Ca, Sr, Ba, Ca$_{0.5}$Sr$_{0.5}$) single crystals; (b) crystal structure of Eu:SrF$_2$ rendered with VESTA software; (c) powder XRD patterns of Eu:AeF$_2$ single crystals and enlarged view of the (111) reflection for Eu:AeF$_2$ (Ae = Ca, Sr, Ba, Ca$_{0.5}$Sr$_{0.5}$) single crystals.

3.1. XRD pattern and ICP results

Powder XRD was carried out on Eu:AeF$_2$ crystals to evaluate how Eu concentration influences the host matrix. As shown in Fig. 1(c), all diffraction peaks coincide with the standard PDF patterns, confirming that Eu incorporation does not change the crystal phase. The (111) reflection was selected to investigate the effect of Eu content on the unit-cell parameter. With increasing Eu concentration, the (111) peak of Eu:AeF$_2$ (Ae = Sr, Ba) shifts to higher 2θ values, the (111) peak of Eu:CaF$_2$ shifts toward lower 2θ angles, indicating lattice expansion. The diffraction angle of Ca$_{0.5}$Sr$_{0.5}$F$_2$ lies between those of CaF$_2$ and SrF$_2$. This is governed by two competing factors. First, Eu^{2+} and Eu^{3+} substitute for Ae^{2+} ions in the matrix [r(Eu^{3+}) = 1.08 Å < r(Ca^{2+}) = 1.12 Å < r(Eu^{2+}) = 1.25 Å < r(Sr^{2+}) = 1.26 Å < r(Ba^{2+}) = 1.42 Å].[50] Second, non-isovalent Eu^{3+} substitution intro-

duces charge-compensating interstitial F^- ions, which can expand the matrix. The observed peak shift therefore reflects the balance between these effects. Although XRD provides a qualitative indication of the Eu^{2+}/Eu^{3+} ratio, precise values were obtained from XPS.

Table 1. Main ion ratio and ICP concentration.

Sample	Proportioning concentration (Eu %mol)	Actual concentration (Eu %mol)
0.3 %mol Eu:CaF_2	0.3	0.26
0.6 %mol Eu:CaF_2	0.6	0.51
1 %mol Eu:CaF_2	1	0.76
0.3 %mol Eu:SrF_2	0.3	0.24
0.6 %mol Eu:SrF_2	0.6	0.45
1 %mol Eu:SrF_2	1	0.77
0.3 %mol Eu:BaF_2	0.3	0.28
0.6 %mol Eu:BaF_2	0.6	0.56
1 %mol Eu:BaF_2	1	0.93
1 %mol Eu:$Ca_{0.5}Sr_{0.5}F_2$	1	0.98
1 %mol Eu:$Ca_{0.33}Sr_{0.33}Ba_{0.33}F_2$	1	0.92

For Eu:$Ca_{0.5}Sr_{0.5}F_2$, all diffraction peaks match those of pure SrF_2, and its matrix constant is closest to that of SrF_2, suggesting that the mixed crystal structurally resembles SrF_2. Overall, all samples crystallize in the cubic $Fm\bar{3}m$ space group and remain single-phase after Eu-doping.

ICP-AES results (Table 1) show that the doping concentrations of Eu^{3+}, Eu^{2+} ions in AeF_2 (Ae = Ca, Sr, Ba, $Ca_{0.5}Sr_{0.5}$, $Ca_{0.33}Sr_{0.33}Ba_{0.33}$) crystals basically match the theoretical doping concentrations, demonstrating good doping uniformity.

3.2. XPS analysis

XPS spectra were collected to determine the valence states and relative concentrations of Eu^{2+}/Eu^{3+} ions in Eu:AeF_2 (Ae = Ca, Sr, Ba) single crystals and are shown in Fig. 2. To accurately determine the relative proportion of Eu^{2+} and Eu^{3+}, we performed detailed curve fitting of the Eu 3d spectra using a combination of a Shirley background and Gaussian–Lorentzian (GL) line shapes. The fitting process considered both the $^3d_{5/2}$ and $^3d_{3/2}$ components.

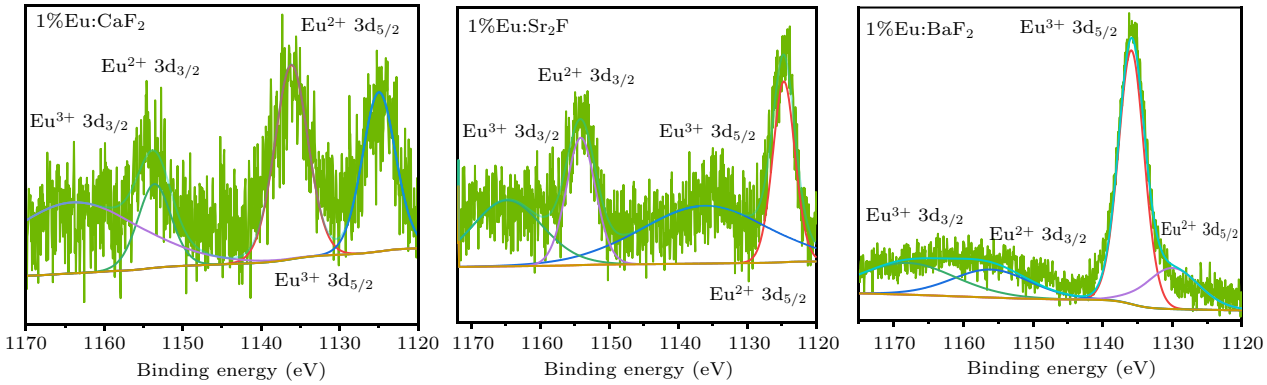


Fig. 2. X-ray phot electron spectroscopy (XPS) curves of 1 %mol Eu:AeF_2 (Ae = Ca, Sr, Ba) sample.

It can be observed that the sample exhibits four photoelectron peaks, located at 1164.3 eV, 1154.6 eV, 1133.2 eV, and 1124.8 eV, which are consistent with reported values in the literature.[51–53] These peaks correspond to the spin-orbit splitting energy levels of (Eu^{3+} $3d_{3/2}$), (Eu^{2+} $3d_{3/2}$), (Eu^{3+} $3d_{5/2}$), and (Eu^{2+} $3d_{5/2}$). The spontaneous reduction of Eu^{3+} to Eu^{2+} in the as-grown alkaline-earth fluoride (AeF_2) single crystals is attributed to a charge compensation mechanism that occurs during the high-temperature crystal growth. In this process, trivalent europium ions from the EuF_3 substitute for the divalent Ae^{2+} cations in the host lattice. To preserve overall charge neutrality, the incorporation of Eu^{3+} ions necessitates the formation of cation vacancies (V_{Ae}), which act as electron donors. Under thermal excitation, electrons from these vacancy defects are transferred to the Eu^{3+} ions, resulting in their reduction to the divalent Eu^{2+} state.

In europium-doped alkaline earth fluorides, the equilibrium between Eu^{2+} and Eu^{3+} oxidation states is highly dependent on the host matrix type and the total doping concentration (Table 2). This dependency is governed by a complex interplay of ionic radius mismatch, the need for charge compensation, and interionic interactions. Crystal-chemical compatibility is a decisive factor: the close ionic radius match between Eu^{2+} (1.25 Å) and Sr^{2+} (1.26 Å) enhances the stability of Eu^{2+} in the SrF_2 matrix, whereas the significant size mismatch in BaF_2 favors the incorporation of the smaller Eu^{3+} (1.08 Å) ion to reduce local matrix strain. Furthermore, as the total europium concentration increases, the proportional concentration of Eu^{3+} rises while that of Eu^{2+} correspondingly decreases, a trend consistent with previous reports in the literature.[54,55]

Table 2. Relationship between the concentrations of Eu^{2+} and Eu^{3+} ions and the variation in Eu ion concentration.

Sample	Eu^{2+} (%mol)	Eu^{3+} (%mol)	Ratios of Eu^{3+}/Eu^{2+}
0.3 %mol Eu:CaF_2	70.90	29.10	0.41
0.6 %mol Eu:CaF_2	62.76	37.24	0.59
1 %mol Eu:CaF_2	57.18	42.82	0.74
0.3 %mol Eu:SrF_2	84.38	15.62	0.18
0.6 %mol Eu:SrF_2	76.33	23.67	0.31
1 %mol Eu:SrF_2	70.10	29.90	0.42
0.3 %mol Eu:BaF_2	24.32	75.68	3.11
0.6 %mol Eu:BaF_2	15.56	84.44	5.42
1 %mol Eu:BaF_2	8.72	91.28	10.46

3.3. Luminescent properties of Eu:AeF_2 single crystals

In Fig. 3, it is clear that the characteristic f–f absorption bands of Eu^{3+} overlap with the broad 4f→5d band of Eu^{2+} within the 280–420 nm range in 1 %mol Eu:AeF_2 single crystals (Ae = Ca, Sr, $Ca_{0.5}Sr_{0.5}$), indicating that Eu^{2+} and Eu^{3+} can be excited simultaneously by wavelengths in this region.

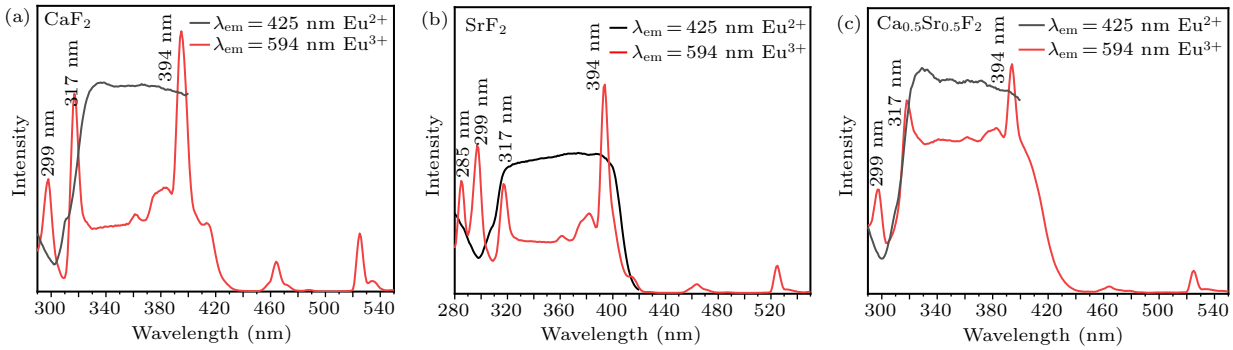


Fig. 3. Excitation spectra of Eu^{2+} (monitoring λ_{em} = 425 nm) and Eu^{3+} (monitoring λ_{em} = 594 nm) in 1 %mol Eu:AeF_2 single crystals (Ae = Ca, Sr, $Ca_{0.5}Sr_{0.5}$).

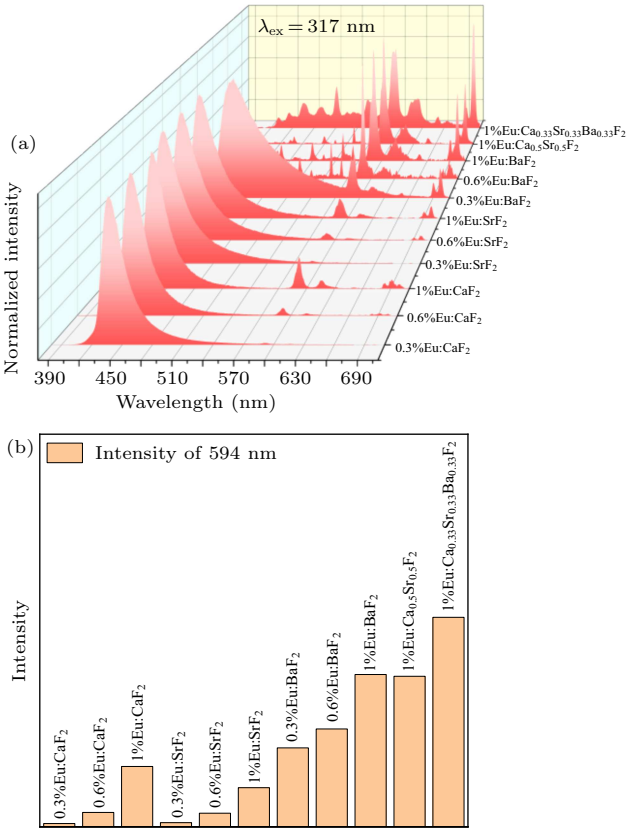


Fig. 4. (a) Normalized emission spectra of Eu:AeF_2 single crystals (Ae = Ca, Sr, $Ca_{0.5}Sr_{0.5}$, $Ca_{0.33}Sr_{0.33}Ba_{0.33}$) excited at 317 nm; (b) variation of the emission intensity at 594 nm for Eu:AeF_2 single crystals (Ae = Ca, Sr, $Ca_{0.5}Sr_{0.5}$, $Ca_{0.33}Sr_{0.33}Ba_{0.33}$).

The room-temperature excitation spectra of Eu:AeF_2 (Ae = Ca, Sr, $Ca_{0.5}Sr_{0.5}$) single crystals are shown in Fig. 4(a). Under 317 nm excitation, all specimens display the characteristic $4f^65d \rightarrow 4f^7$ broadband of Eu^{2+} (400–550 nm) together with the sharp $^5D_0 \rightarrow {}^7F_J$ lines of Eu^{3+} (585–710 nm). The Eu^{2+} maximum migrates from 440 nm in CaF_2 to 455 nm in SrF_2 and to 485 nm in BaF_2, a red shift with increasing cationic radius. Although the cubic AeF_2 matrix field (CN = 8) weakens from Ca^{2+} to Ba^{2+}, the 5d level is lowered and the transition energy decreases. In Fig. 4(b), the Eu^{3+} lines mirror this trend, the dual-cation $Ca_{0.5}Sr_{0.5}F_2$ and the medium-entropy $Ca_{0.33}Sr_{0.33}Ba_{0.33}F_2$ single crystals exhibit a markedly broadened Eu^{2+} band with a multi-peak profile. Random occupation of the cation submatrix generates a distribution of local Eu–F bond lengths and thus a spectrum of micro-crystal fields, leading to broadened emission. The data evidence a monotonic red shift and intensity gain of Eu^{2+} emission with increasing host polarizability, a progressive strengthening of crystal field splitting from CaF_2 to BaF_2, and pronounced entropy-induced line broadening in multi-cation fluorides.

3.4. Changes in the local matrix structure of Eu ions

The $^5D_0 \rightarrow {}^7F_1$ transition of Eu^{3+} is a magnetic-dipole transition and is comparatively insensitive to the local environment, whereas the $^5D_0 \rightarrow {}^7F_2$ transition is an electric-dipole transition that is highly environment-sensitive. The intensity ratio $R = I(^5D_0 \rightarrow {}^7F_2)/I(^5D_0 \rightarrow {}^7F_1)$ reflects the strength of the chemical bonds and the symmetry around Eu^{3+} ions.[56,57] A higher R value indicates a higher degree of disorder and lower symmetry in the surrounding matrix, which enhances 4f–4f level splitting and gives a stronger emission intensity. As shown in Fig. 5, the R values obtained from Eu:AeF_2 (Ae = Ca, Sr, Ba) increase with rising Eu content, indicating that local

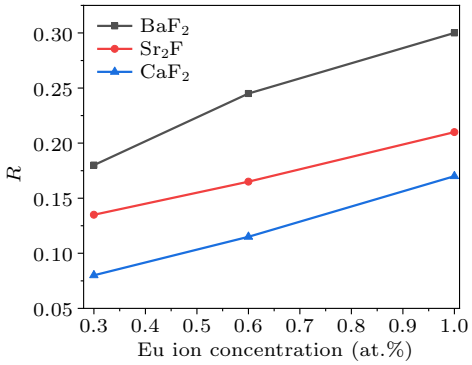


Fig. 5. Integrated intensity ratio $R = I(^5D_0 \rightarrow {}^7F_2)/I(^5D_0 \rightarrow {}^7F_1)$ of Eu:AeF_2 single crystals (Ae = Ca, Sr, Ba).

symmetry around Eu^{3+} decreases as the Eu concentration increases in AeF_2. Regarding the host effect, Eu^{3+} experiences lower symmetry in BaF_2 than in CaF_2 or SrF_2.

3.5. Fluorescence lifetime

The fluorescence lifetimes of the Eu^{3+} $^5D_0$ and Eu^{2+} emitting levels in Eu:AeF_2 single crystals (Ae = Ca, Sr, Ba, $Ca_{0.5}Sr_{0.5}$) were measured at room temperature, For Eu:AeF_2, the Eu^{3+} $^5D_0$ decay curves are well described by a single-exponential function

$$I(t) = I_0 \exp\left(\frac{-t}{\tau}\right), \tag{1}$$

where $I(t)$ is the luminescence intensity at time t after the excitation is switched on, I_0 is the initial intensity ($t = 0$), and τ is the lifetime.

The Eu^{2+} decay curves are non-exponential, and the effective average lifetime τ is derived using[57,58]

$$\tau_{avg} = \frac{\int_0^\infty tI(t)\,dt}{\int_0^\infty I(t)\,dt}. \tag{2}$$

From Fig. 6 and Table 3, it is evident that, as the Eu concentration increases, the Eu^{2+} decay lifetime changes in the opposite direction to that of Eu^{3+}. The Eu^{2+} lifetime decreases from 106.3 ns to 84.4 ns in CaF_2 and from 168.7 ns to 114.2 ns in SrF_2; decreases from 143.9 ns to 114.5 ns in BaF_2.

In contrast, the fluorescence lifetime of the Eu^{2+} ions, shown in Fig. 6(b), displays an opposite and decreasing trend across the same host crystal series. This behavior is compelling evidence of an efficient energy transfer (ET) mechanism from Eu^{2+} to Eu^{3+}. This enhancement in ET efficiency is likely governed by the improved spectral overlap between the donor (Eu^{2+}) emission and acceptor (Eu^{3+}) absorption. The expansion of the matrix from CaF_2 to BaF_2 modifies the crystal field environment, which can lower the energy of the broad $4f^65d^1$ excited state of Eu^{2+}, causing its emission band to better overlap with the $^7F_0 \rightarrow {}^5D_j$ absorption lines of Eu^{3+}.

Table 3. Eu:AeF_2 single crystals (Ae = Ca, Sr, Ba) fluorescence lifetimes.

Sample	Fluorescence lifetimes (Eu^{2+})	Fluorescence lifetimes (Eu^{3+})
0.3 %mol Eu:CaF_2	106.3 ns	11.38 ms
0.6 %mol Eu:CaF_2	93.7 ns	12.26 ms
1 %mol Eu:CaF_2	84.4 ns	14.31 ms
0.3 %mol Eu:SrF_2	168.7 ns	13.02 ms
0.6 %mol Eu:SrF_2	132.5 ns	14.21 ms
1 %mol Eu:SrF_2	114.2 ns	15.38 ms
0.3 %mol Eu:BaF_2	143.9 ns	13.36 ms
0.6 %mol Eu:BaF_2	121.6 ns	14.72 ms
1 %mol Eu:BaF_2	114.5 ns	16.42 ms

3.6. Energy transfer process between Eu^{2+} and Eu^{3+}

The emission (λ_{em} = 594 nm) and excitation (λ_{ex} = 299 nm) spectra of 1 %mol Eu:AeF_2 single crystals (Ae = Ca, Sr, Ba, $Ca_{0.5}Sr_{0.5}$) are shown in Fig. 7. All four hosts display considerable spectral overlap between the Eu^{3+} f–f bands and the Eu^{2+} 4f→5d band, and the opposite lifetime trends of Eu^{3+} and Eu^{2+} confirm $Eu^{2+} \rightarrow Eu^{3+}$ energy transfer. In Fig. 7, this overlap is especially pronounced for Eu:$Ca_{0.5}Sr_{0.5}F_2$, whose mixed matrix enhances $4F^-$ level splitting for both valence states, intensifying their emissions and strengthening the transfer process.

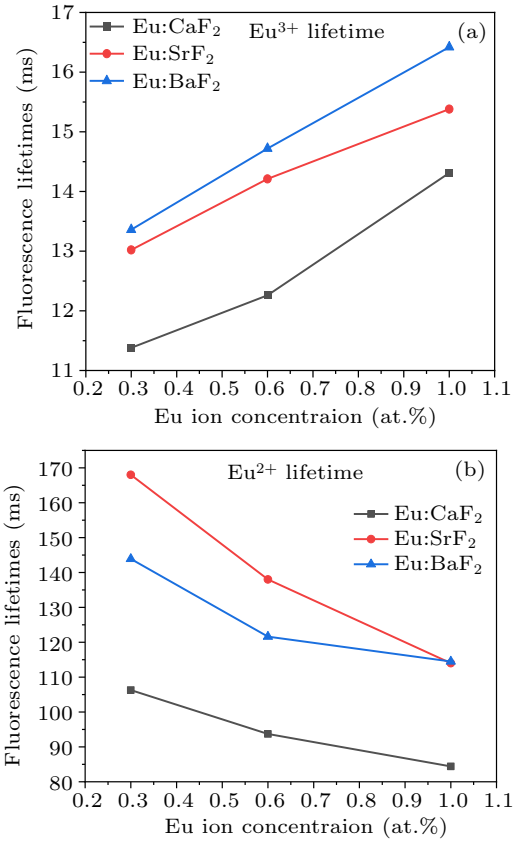


Fig. 6. (a) Fluorescence lifetime variation tendencies of the Eu^{3+} $^5D_0$ energy level in Eu:AeF_2 single crystals (Ae = Ca, Sr, Ba). (b) Fluorescence lifetime variation tendencies of the Eu^{2+} energy level.

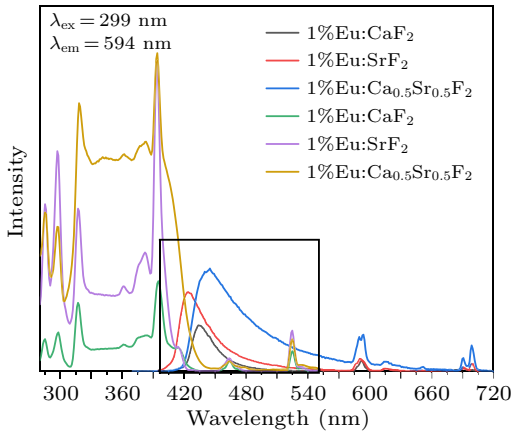


Fig. 7. Emission spectra under 299 nm excitation and excitation spectra monitored at 594 nm for 1 %mol Eu:AeF_2 single crystals (Ae = Ca, Sr, $Ca_{0.5}Sr_{0.5}$, $Ca_{0.33}Sr_{0.33}Ba_{0.33}$).

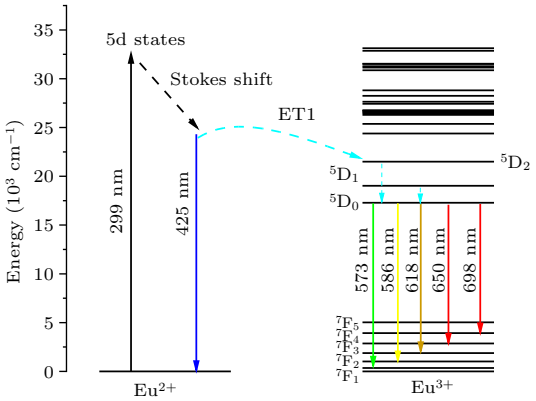


Fig. 8. Schematic illustration of $Eu^{2+} \rightarrow Eu^{3+}$ energy-transfer pathways.

Based on these observations, two energy-transfer channels are proposed and summarized in Fig. 8. Under 290 nm UV excitation, Eu^{2+} ions in Eu-doped AeF_2 single crystals (Ae = Ca, Sr, $Ca_{0.5}Sr_{0.5}$) are promoted from the $4f^7$ ground state to the parity-allowed $4f^65d^1$ configuration and relax nonradiatively to the lowest 5d crystal-field sublevel. Two decay pathways then emerge: (1) an intrinsic $4f^65d^1 \rightarrow 4f^7$ transition that yields a broad blue emission band centred at 425 nm, and (2) resonant $Eu^{2+} \rightarrow Eu^{3+}$ energy transfer enabled by the spectral overlap between this band (390–470 nm) and the Eu^{3+} $^5D_{1,2}$ absorptions. The transferred energy in Eu^{3+} relaxes from $^5D_2$ to the long-lived $^5D_0$ level, which emits narrow $^5D_0 \rightarrow {}^7F_J$ (J = 0–4) lines at 573 nm, 586 nm, 618 nm, 650 nm, and 698 nm, thereby converting near-UV photons into red light.

As an efficient energy transfer (ET) from a donor (Eu^{2+}) to an acceptor (Eu^{3+}) introduces a competing decay channel, it invariably shortens the donor's fluorescence lifetime, making this parameter a direct probe of ET efficiency. Table 4 provides compelling quantitative evidence for this phenomenon by presenting the ratio of the Eu^{2+} lifetime at higher dopant levels (0.6 %mol and 1 %mol) relative to a 0.3 %mol baseline. Across all host matrices (CaF_2, SrF_2, and BaF_2), the data reveals a systematic decrease in this ratio as the total Eu concentration increases; for example, in the SrF_2 host, the lifetime ratio drops from 0.78 at 0.6 %mol Eu to 0.67 at 1 %mol Eu. This consistent and marked reduction in the Eu^{2+} lifetime proves that the energy transfer efficiency is substantially boosted at higher doping levels, a result attributed to the decreased average distance between donor-acceptor ions and the increased population of Eu^{3+} acceptors, which greatly accelerates the transfer rate.

Table 4. Ratio of the Eu^{2+} lifetime at higher dopant levels (0.6 %mol and 1 %mol) relative to a 0.3 %mol baseline of Eu:AeF_2 single crystals (Ae = Ca, Sr, Ba) $\tau(Eu^{2+})$.

Sample	$\tau(Eu^{2+})/\tau(Eu^{2+}$ 0.3 %mol Eu doping)
0.6 %mol Eu:CaF_2	0.88
1 %mol Eu:CaF_2	0.79
0.6 %mol Eu:SrF_2	0.78
1 %mol Eu:SrF_2	0.67
0.6 %mol Eu:BaF_2	0.84
1 %mol Eu:BaF_2	0.79

3.7. CIE chromaticity coordinates of Eu:AeF_2 samples

Excitation (λ_{ex} = 299 nm) spectra of 1 %mol Eu:AeF_2 single crystals (Ae = Ca, Sr, Ba, $Ca_{0.5}Sr_{0.5}$) are shown in Fig. 9(a). Under 299 nm excitation, all Eu-doped alkaline-earth fluorides exhibit the broad Eu^{2+} $4f^65d^1 \rightarrow 4f^7$ band superimposed on the sharp Eu^{3+} $^5D_0 \rightarrow {}^7F_J$ lines, yet the Eu^{2+}/Eu^{3+} emission ratio varies markedly with host. In SrF_2, the Eu^{2+} band is both strongest and narrowest, indicating the optimal stabilization of Eu^{2+} by the Sr^{2+} matrix. CaF_2 likewise favors Eu^{2+} emission, though with a slightly broader profile. Introducing cation disorder progressively suppresses Eu^{2+} in $Ca_{0.5}Sr_{0.5}F_2$ the blue band widens and weakens while Eu^{3+} lines emerge, and in the fully mixed $Ca_{0.33}Sr_{0.33}Ba_{0.33}F_2$ the two valence states emit with comparable intensity. In BaF_2, the Eu^{3+} transitions dominate, showing that the larger, more polarizable BaF_2 matrix disfavors electron trapping by Eu. In Fig. 9(b), monitoring the emission at 593 nm reveals four excitation peaks for 1 %mol Eu:$Ca_{0.33}Sr_{0.33}Ba_{0.33}F_2$, centered at 286 nm, 299 nm, 318 nm, and 393 nm. Taking these wavelengths as excitation sources, Fig. 9(c) shows that Eu^{2+} and Eu^{3+} emissions coexist in the same crystal, and their relative intensities change markedly with excitation wavelength. Deep-UV excitation at 286 nm yields only weak

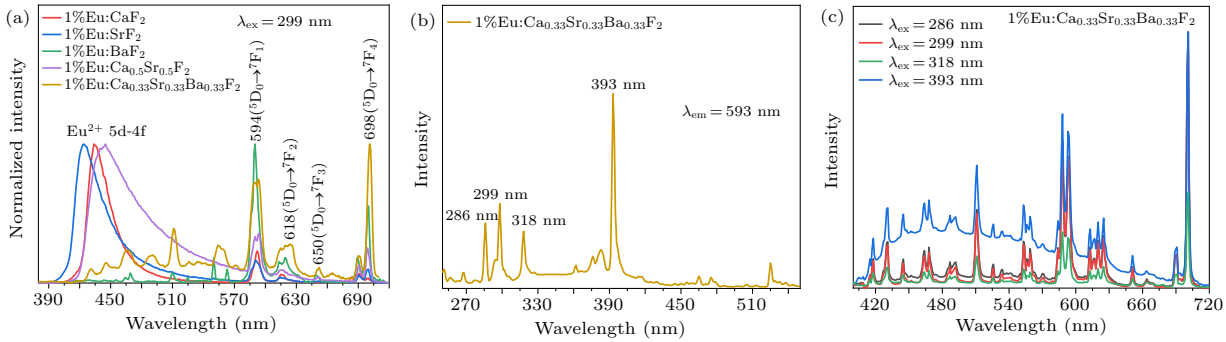


Fig. 9. (a) Normalized emission spectra under 299 nm excitation and excitation spectra monitored at 594 nm for 1 %mol Eu:AeF_2 single crystals (Ae = Ca, Sr, $Ca_{0.5}Sr_{0.5}$, $Ca_{0.33}Sr_{0.33}Ba_{0.33}$). (b) Excitation spectrum recorded by monitoring the 593 nm emission of 1 %mol Eu:$Ca_{0.33}Sr_{0.33}Ba_{0.33}F_2$ single crystals. (c) Emission spectra of 1 %mol Eu:$Ca_{0.33}Sr_{0.33}Ba_{0.33}F_2$ single crystals recorded under excitation wavelengths of 286 nm, 299 nm, 318 nm, and 393 nm.

emission. When the excitation wavelength shifts to 299 nm or 318 nm, the overall luminescence intensifies. Under 393 nm excitation, the Eu^{3+} emission lines strengthen while the Eu^{2+} band weakens. Thus, by simply tuning the excitation wavelength, multicolor emission can be achieved in the 1 %mol Eu:$Ca_{0.33}Sr_{0.33}Ba_{0.33}F_2$ single crystal.

3.8. CIE chromaticity coordinates of 1 %mol Eu:AeF_2 single crystals

Figure 10 shows how the CIE 1931 x–y chromaticity coordinates of alkaline-earth fluorides co-doped with 1% mol Eu^{2+}/Eu^{3+} evolve with host composition under 299 nm excitation. The emission color drifts systematically from deep-blue CaF_2 (0.1720, 0.0382), through bluish-white SrF_2 (0.1825, 0.0754) and $Ca_{0.5}Sr_{0.5}F_2$ (0.2023, 0.1609), to warm-white $Ca_{0.33}Sr_{0.33}Ba_{0.33}F_2$ (0.4018, 0.3644) and BaF_2 (0.4135, 0.3516). This red-shift of the Eu^{2+} $4f^65d^1 \rightarrow 4f^7$ band with increasing average cation radius originates from the concomitant reduction in 5d crystal-field splitting, while the narrow Eu^{3+} $^5D_0 \rightarrow {}^7F_J$ lines add a red component that further modulates the overall chromaticity.

The quaternary solid solution $Ca_{0.33}Sr_{0.33}Ba_{0.33}F_2$ displays pronounced excitation-dependent tunability. Upon 318 nm and 393 nm excitation, its chromaticity coordinates shift to (0.3145, 0.3372) and (0.3693, 0.3435), corresponding to the correlated color of neutral white and warm white, respectively. The combined broadband Eu^{2+} emission and line-like Eu^{3+} emission thus afford single-phase white-light generation that can be tuned solely by the excitation wavelength, without auxiliary activators.

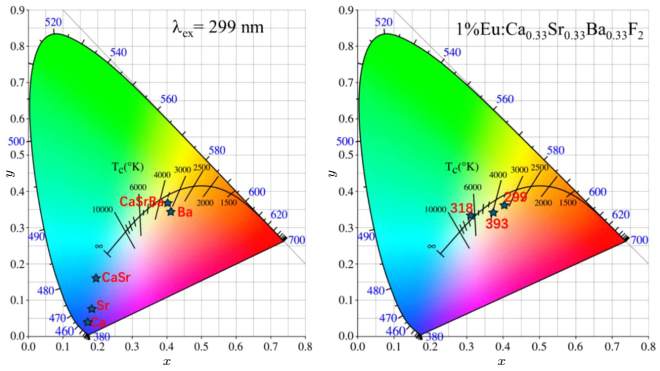


Fig. 10. (a) CIE 1931 chromaticity coordinates of 1 %mol Eu:AeF_2 single crystals (Ae = Ca, Sr, Ba, and $Ca_{0.5}Sr_{0.5}$, $Ca_{0.33}Sr_{0.33}Ba_{0.33}$) under 299 nm excitation; (b) 1 %mol Eu:$Ca_{0.33}Sr_{0.33}Ba_{0.33}F_2$ under 299 nm, 318 nm, and 393 nm excitation.

Table 5 summarizes the characteristics of 1 mol% Eu-doped alkaline earth fluoride (AeF_2) single crystals. The data highlight that the cation composition of the host matrix has a profound impact on the structural and luminescent properties of the Eu^{2+} activating ions. As expected, mixed-cation crystals, particularly the medium-entropy crystal Eu:$Ca_{0.33}Sr_{0.33}Ba_{0.33}F_2$, exhibit the lowest local symmetry due to the random distribution of cations with different sizes. This reduction in symmetry can enhance the splitting strength of Eu^{3+} ion energy levels, thereby boosting the emission intensity of Eu^{3+} ions.

This is confirmed by the CIE 1931 chromaticity coordinates (x, y). The emission color shifts from deep blue in host matrices with higher symmetry to white in those with lower local symmetry. Reducing the local symmetry around the Eu^{3+} dopant ions through a medium-entropy approach is an effective strategy for simultaneously enhancing emission intensity and tuning the emission color.

Table 5. Summary of the properties of 1% mol Eu-doped AeF_2 single crystals.

Sample	R	CIE (x, y)
Eu:CaF_2	0.17	(0.172, 0.0382)
Eu:SrF_2	0.21	(0.1825, 0.0754)
Eu:BaF_2	0.30	(0.4135, 0.3516)
Eu:$Ca_{0.5}Sr_{0.5}F_2$	0.28	(0.2023, 0.1609)
Eu:$Ca_{0.33}Sr_{0.33}Ba_{0.33}F_2$	0.37	(0.4018, 0.3644)

4. Conclusions

High-quality Eu-doped CaF_2, SrF_2, BaF_2, $Ca_{0.5}Sr_{0.5}F_2$, and $Ca_{0.33}Sr_{0.33}Ba_{0.33}F_2$ single crystals were successfully grown by the vertical Bridgman technique without secondary phases. XPS confirmed the coexistence of Eu^{2+} and Eu^{3+}; the Eu^{2+}/Eu^{3+} fraction decreases with dopant concentration in AeF_2. Indicating a pronounced host-dependent redox equilibrium. Photoluminescence measurements reveal a broad Eu^{2+} $4f^65d^1 \rightarrow 4f^7$ emission band (400–550 nm) that red-shifts and broadens gradually from CaF_2 (440 nm) to BaF_2 (485 nm), whereas the narrow Eu^{3+} $^5D_0 \rightarrow {}^7F_J$ lines (585–710 nm) remain essentially host-independent. The substantial spectral overlap between Eu^{2+} emission and Eu^{3+} excitation, together with opposite lifetime trends, demonstrates efficient $Eu^{2+} \rightarrow Eu^{3+}$ resonant energy transfer that can be tuned by matrix symmetry.

Under 299 nm excitation, the chromaticity coordinates can be continuously tuned from deep blue CaF_2 (0.1720, 0.0382) through bluish white (SrF_2 and $Ca_{0.5}Sr_{0.5}F_2$) to warm white BaF_2 (0.4135, 0.3516). In the medium-entropy solid solution $Ca_{0.33}Sr_{0.33}Ba_{0.33}F_2$, the emission color can even be reversibly switched from neutral to warm white merely by changing the excitation wavelength.

In summary, host-controlled Eu^{2+}/Eu^{3+} redox balance and energy transfer provide a single-activator route to wide-gamut, excitation-tunable luminescence, and multi-cation fluorides introduce additional bandwidth and color-rendering degrees of freedom. These findings supply valuable guidelines for the design of next-generation self-activated multicolor phosphors and single-phase white emitters for solid-state lighting and display technologies.

Acknowledgements

This work is partially supported by the National Key Research and Development Program of China (Grant Nos. 2022YFB3605701 and 2023YFB3507401) and the National Natural Science Foundation of China (Grant Nos. 62275198, 62075166, and 62450134).

References

[1] Du P, Huang X Y and Yu J S 2018 *Chem. Eng. J.* **337** 91
[2] van de Haar M A, Werner J, Kratz N, Hilgerink T, Tachikirt M, Honold J and Krames M R 2018 *Appl. Phys. Lett.* **112** 132101
[3] Jha K and Simhadri M J 2017 *J. Am. Ceram. Soc.* **100** 1402
[4] Li X, Zhong H, Chen B, Sui G, Sun J, Xu S, Cheng L and Zhang J 2018 *Opt. Express* **26** 1870
[5] Pawlik N, Sapkowski-Sroka B, Goryczka T, Zubko M, Lelątko J and Pisarski W A 2019 *J. Eur. Ceram. Soc.* **39** 5010
[6] Tong Y, Jin M, Chen Y, Zhao Y, Yang H, Wang Q, Zhai L, Liang X and Xiang W 2021 *J. Mater. Chem. C* **9** 2530
[7] Zeng X, Yu L, Peng K, Yu Y, Sun D, Miao C H and Fu Y 2023 *J. Lumin.* **261** 119910
[8] Feinle A, Lavoie-Cardinal F, Akbarzadeh J, Peterlik H, Adlung M, Wickleder C and Hüsing N 2012 *Chem. Mater.* **24** 3674
[9] Popov P A, Dukelski K V, Mironov I A, Smirnov A N, Smolyanskiĭ P L, Fedorov P P, Osiko V V and Basiev T T 2007 *Dokl. Phys.* **52** 7
[10] Afshani J, Delgado T, Paveliuc G and Hagemann H 2022 *J. Lumin.* **246** 118805
[11] Zhao F, Song Z and Liu Q 2021 *Inorg. Chem.* **60** 3952
[12] Amin M R, Strobel P, Schnick W, Schmidt P J and Moewes A 2022 *J. Mater. Chem. C* **10** 9740
[13] Liao M, Wu F, Zhu D, Zhang X, Dong H, Lin Z, Wen M and Mu Z 2022 *Chem. Eng. J.* **449** 137801
[14] Zhao M, Yang Z, Ning L and Xia Z 2021 *Adv. Mater.* **33** 2101428
[15] Xu H, Jing W, Liu M, Yin M and Duan C K 2023 *Phys. Rev. B* **107** 075145
[16] Yuan R R, Liu J M, Zhang H L, Zhang Z L, Shao G Z, Liang X J and Xiang W D 2018 *J. Am. Ceram. Soc.* **101** 4927
[17] Nogami M, Yamazaki T and Abe Y 1998 *J. Lumin.* **78** 63
[18] Wu H, Xu M and Chang C 2024 *J. Alloys Compd.* **1002** 175430
[19] Zuo Y, She C F, Liu X Y, Huang W and Gong Y 2025 *Sep. Purif. Technol.* **361** 131572
[20] Pei Z, Zeng Q and Su Q 2000 *J. Phys. Chem. Solids* **61** 9
[21] Grandhe B K, Bandi V R, Jang K, Kim S S, Shin D S, Lee Y I, Lim J M and Song T 2011 *J. Alloys Compd.* **509** 7937
[22] Rezende M V d S, Valerio M E and Jackson R A 2015 *Mater. Res. Bull.* **61** 348
[23] Huang S, Shang M, Yan Y, Dang P and Lin J 2022 *Inorg. Chem.* **61** 1756
[24] Barbin V, Jouart J P and D'Almeida T 1996 *Chem. Geol.* **130** 77
[25] George G, Hayes J I, Collins C N, Davis J E, Yu L, Lin Y, Wen J, Ila D and Luo Z 2021 *J. Alloys Compd.* **857** 157591
[26] Pandey C, Dhopte S, Muthal P, Kondawar V and Moharil S 2007 *Radiat. Eff. Defect. Solids* **162** 651
[27] Sibley W, Hunt C and Spaeth J 1988 *J. Lumin.* **42** 35
[28] Luo Q, Qiao X, Fan X and Zhang X 2010 *J. Am. Ceram. Soc.* **93** 2684
[29] Zhu Y, Xu Z, Luo Q, Feng S, Liu X and Li L 2020 *Ceram. Int.* **46** 560
[30] Kawano K, Katoh K and Nakata R 1997 *J. Phys. Soc. Jpn.* **66** 1803
[31] Wang C, Wang D, Xu X, Li P, Zhao J, Qian G and Fan X 2022 *J. Mater. Chem. C* **10** 16138
[32] de Mesquita B R, Rezende M V d S and dos Santos M A C 2021 *J. Lumin.* **238** 118297
[33] Hamers R, Wietfeldt J and Wright J 1982 *J. Chem. Phys.* **77** 683
[34] Sun J, Zhang Y, Zheng Y, Xu Z and Liu R 2014 *Thin Solid Films* **562** 478
[35] Cortelletti P, Pedroni M, Boschi F, Pin S, Ghigna P, Canton P, Vetrone F and Speghini A 2018 *Cryst. Growth Des.* **18** 686
[36] Bebars S, Gadallah A S, Khedr M A and Abou Kana M T 2017 *J. Lumin.* **192** 949
[37] Zhang X, Hayakawa T, Nogami M and Ishikawa Y 2011 *J. Alloys Compd.* **509** 2076
[38] Ratnakaram Y, Balakrishna A and Rajesh D 2012 *Phys. B* **407** 4303
[39] Zhang X, Hayakawa T, Ishikawa Y, Yang L and Nogami M 2015 *J. Alloys Compd.* **644** 77
[40] Zheng T, Runowski M, Woźny P and Lis S 2020 *J. Alloys Compd.* **822** 153511
[41] Ingham R, van der Heijden C, Budwilowitz K, Niehe M, Dugulan I and Hintzen H T 2024 *Adv. Opt. Mater.* **12** 2401738
[42] Wang F, Chen H, Zhang S, Zhang S and Jin H 2023 *J. Alloys Compd.* **969** 172394
[43] Chen W, Ouyang Y and Mo M 2022 *J. Am. Ceram. Soc.* **105** 2646
[44] Dai W 2014 *J. Mater. Chem. C* **2** 3951
[45] Tsuboi T and Qiao X 2023 *ECS J. Solid State Sci. Technol.* **12** 066007
[46] Malchukova E and Boizot B 2010 *Mater. Res. Bull.* **45** 1299
[47] Zaitoun M, Goken D, Bailey L, Kim T and Lin C 2000 *J. Phys. Chem. B* **104** 189
[48] Baran A, Barzowska J, Grinberg M, Mahlik S, Szczodrowski K and Zorenko Y 2013 *Opt. Mater.* **35** 2107
[49] Jiang W, Fu R, Gu X, Zhang P and Coşgun A 2015 *J. Lumin.* **157** 46
[50] Jia Y 1991 *J. Solid State Chem.* **95** 184
[51] Bezrkovnyi O, Vorokhta M, Małecka M, Mista W and Kepinski L 2020 *Catal. Commun.* **135** 105875
[52] Le F, Wang L, Jia W, Jia D and Bao S 2012 *J. Alloys Compd.* **512** 323
[53] Wu H, Yang X, Yu X, Liu J, Yang H, Lv H and Yin K 2009 *J. Alloys Compd.* **480** 867
[54] Ahlawat R, Rani N and Goswami B 2018 *J. Alloys Compd.* **743** 126
[55] Chen B, Li C, Deng D, Ruan F, Wu M, Wang L, Zhu Y and Xu S 2019 *J. Alloys Compd.* **792** 702
[56] Watanabe Y, Hiruma Y, Nagata H and Takenaka T 2008 *Ceram. Int.* **34** 761
[57] DeShazer L and Dieke G 1963 *J. Chem. Phys.* **38** 2190
[58] Chang N and Gruber J 1964 *J. Chem. Phys.* **41** 3227